Int J Fract (2017) 205:37–56
DOI 10.1007/s10704-017-0180-8

ORIGINAL PAPER

Investigation of viscoelastic fracture fields in asphalt mixtures using digital image correlation

Berangere Doll · Hasan Ozer · Jose J. Rivera-Perez · Imad L. Al-Qadi · John Lambros

Received: 3 March 2016 / Accepted: 3 January 2017 / Published online: 27 January 2017

Abstract In this work we have studied the fracture behavior of asphalt mixtures, a heterogeneous mix of hard aggregates (usually in the form of crushed quarried rock) with a petroleum based asphalt binder, used in paving applications. Specifically, we studied the dependence of asphalt mixes' fracture response on loading rate, temperature, and recycled content—the latter used primarily to replace virgin materials like aggregates and binder. Fracture tests were conducted on semi-circular bend edge cracked specimens obtained from mixes with different compositions, and the fracture event was recorded with a camera to allow for digital image correlation (DIC) measurements. DIC, with a spatial resolution of about 40 μm/pixel, measured the far-field strain and displacement fields developing around a preexisting notch tip. Our focus here is on characterizing the material behavior by quantifying its viscoelastic response and fracture properties. The elastic–viscoelastic correspondence principle was used to extract viscous and elastic components from the full-field DIC-measured strain and displacement fields. Various energy dissipation mechanisms other than the fracture itself were evaluated. Stress–strain response and energy dissipated in the far-field regions were quantified. The pseudo-elastic stress intensity factor was then used to study the fracture properties, and quantify the effects on fracture properties of loading rate, temperature, and recycled content in the binder. It was seen that the viscoelastic characteristics of the material were a dominant factor in the material behavior obtained at room temperature. In general, the elastic component of the displacement was only up to about 30% of the total displacement, indicating a strong influence of viscoelasticity in this state. Loading rate, temperature and recycled asphalt shingles (RAS) content all affected the viscous response by introducing more elastic response when loading rate or recycled content increased or when temperature decreased. It became clear from these macroscopic measurements that the increase of RAS content considerably embrittles the material producing less viscous effects and less energy dissipated in the far-field, almost comparable to reductions associated with the loading rate increase (from 6.25 to 50 mm/min) or the temperature change (−12 to 25 °C).

Keywords Asphalt concrete mixtures · Viscoelasticity · Recycled asphalt shingles (RAS) · Digital image correlation (DIC) · Fracture · Semi-circular bend (SCB)

B. Doll · J. Lambros (✉)
Aerospace Engineering, University of Illinois Urbana-Champaign, 306 Talbot Lab, 104 S. Wright St., Urbana, IL 61801, USA
e-mail: lambros@illinois.edu

H. Ozer · J. J. Rivera-Perez · I. L. Al-Qadi
Civil and Environmental Engineering, University of Illinois Urbana-Champaign, Urbana, IL 61801, USA

1 Introduction

Asphalt concrete (AC) mix is a composite material made of aggregates and binder. Aggregates are usually a hard phase, like rock quarried from the ground and processed to specific size and gradations, and amount to volume fractions of up to 85% of the mix. Asphalt binder, constituting about 5–10% by volume of the AC mixes, acts as the binding matrix material. The pavement industry is currently interested in increasing the amount of recycled content in AC as it both reduces the material cost and provides an environmentally friendlier product. Note that both elements of the AC mix can include some recycled material. Two commonly used recycled materials are reclaimed asphalt pavement (RAP) or recycled asphalt shingles (RAS) replacing virgin aggregates and asphalt binder. Aggregates can also be replaced with steel slag for example, which is a waste product of the steel industry (Ahmedzade and Sengoz 2009). RAP is obtained through cold milling or crushing of old AC pavement while RAS is obtained from the grinding of shingles (Osman 2014). There are two types of RAS: the first is manufacturer waste which is made of asphalt roofing shingles that were never used as they were rejected by the manufacturer, while the second type of RAS is called tear-off and is obtained from shingles removed from roofs (Osman 2014) and have thus been exposed to years of weathering. For mixtures containing RAS or RAP, some of the binder contained in the recycled material may blend with the original binder, but the extent of blending and stiffness of the recycled binder is variable (Goh and You 2011; Zhao et al. 2014). Even though blending of original virgin binder and recycled binder is variable and unknown, it is assumed that virgin binder is fully replaced by recycled binder by weight resulting in significant cost reductions due to decreased use of virgin asphalt binder. The ratio of virgin asphalt binder replaced by recycled binder is known as the asphalt binder replacement (ABR) percentage.

The primary motivation of using RAS and RAP in pavement is upfront economic savings because of reduced material production costs. The inherent assumption herein is that the performance of AC mixtures with addition of RAP and RAS is not compromised. Clearly, this is a valid replacement approach only if the performance of the AC mixes with recycled materials is equivalent to that of mixes with a virgin binder. Investigating this issue is legitimate since the binder extracted from recycled materials is aged, meaning that it is likely stiffer, and the amount of blending of the recycled binder with virgin binder is not well known. Studies on ABR have shown that it can reduce high temperature rutting and plastic permanent deformation which are related to the increased stiffness of the AC mix (Goh and You 2011; Ozer et al. 2012). However ABR may degrade performance of low temperature strength and thermal cracking and intermediate fatigue cracking (Newcomb et al. 1993; Johnson et al. 2010) as an increased stiffness of the AC mix can also mean that the material is more brittle thus vulnerable to cracking. As a result, when a mix contains high amounts of recycled content, often a softer and more flexible binder is used [represented by a reduction in its binder's performance grade (PG) such as from PG 64-22 to PG 58-28] to compensate for the stiffening of the aged binder (Osman 2014). This is commonly done in an ad hoc manner since the detailed effect of recycled content on material fracture response remains unknown.

Other parameters that are not linked to chemical composition, such as aging or moisture, are known to have an impact on the mechanical behavior of the material (Petersen and Harnsberger 2007; Gorkem and Sengoz 2009), although they are not directly of interest here. However, as asphalt is a viscoelastic material, the response of the material is time dependent and parameters such as temperature and loading rate affect its behavior. An increase in temperature or a decrease in loading rate induces a more compliant response of the material. These elements show that many factors influence the characteristics of asphalt, possibly in a coupled and connected fashion, and continued work is necessary to understand how each parameter impacts the material properties—in this particular case fracture properties are of interest.

The work presented herein aims at improving our understanding of the fracture behavior of AC in particular by evaluating the effects of RAS, loading rate and material temperature on the fracture response of AC composites. To study these aspects of AC fracture, we will be performing bend fracture tests on AC mixes containing different levels of RAS while varying the loading rate at both low (−12 °C) and intermediate (25 °C) temperatures. Studies on AC are usually based on experiments that measure the global response of a specimen, for example far-field applied displacement and load measurements. Here, however, to complement the data traditionally obtained from far-field load

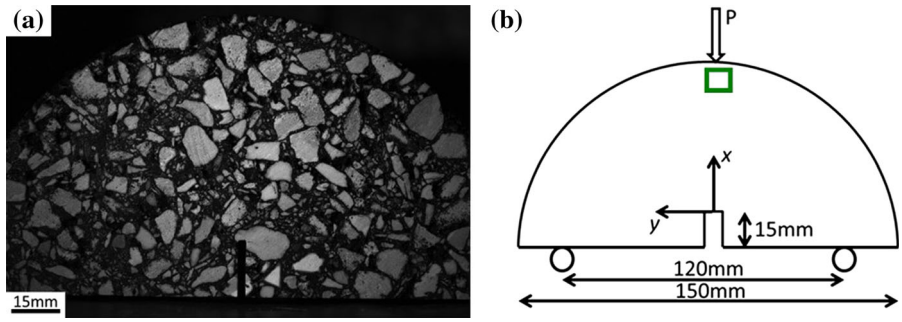

Fig. 1 **a** Optical micrograph of asphalt SCB specimen showing aggregate particles (*white*) and binder matrix (*black*). Notch is also visible at the bottom surface. **b** Schematic and dimensions of SCB 3-point bend test. *Green square* is used to measure LLD from DIC

and displacement measurements we will use the digital image correlation (DIC) technique which enables full-field measurements by taking successive pictures of a random speckle pattern on the surface of a specimen while it is deformed and comparing the pictures before and after deformation to compute in-plane displacements and strains (Sutton et al. 2009). The DIC technique presents several advantages as it is a non-contact technique, gives measurements on the entire surface of the specimen, and has relatively easy preparation since it only requires a speckle pattern to be applied on the specimen surface. The method has been successfully used for a variety of materials including asphalt (Masad et al. 2001; Seo et al. 2002; Buttlar et al. 2014). The aim of this work is to use the DIC displacement and strain measurements to assess the viscoelastic effects developing in the material during fracture and how these depend on RAS content, rate and temperature. The behavior at the far-field will also be analyzed to understand how it is affected by the propagation of the crack and its contribution to the overall behavior of the material (energy dissipation).

2 Experimental techniques

2.1 Material and sample preparation

Asphalt concrete is a viscoelastic and heterogeneous material made of aggregates (approximately 85% by volume), asphalt binder (approximately 5–10% by volume), and air voids. The binder, a compliant product of petroleum refinery operations containing hydrocarbon chains, is also referred to as asphalt. Asphalt binder behavior is considered viscoelastic (highly temperature and rate dependent) and is the cementing or binding agent between the solid aggregates typically considered (linearly) elastic and brittle and obtained from different parent rock materials such as limestone, quartzite, sandstone, granite, and basalt. The matrix viscoelastic response, however, translates to a viscoelastic response of the overall AC mixture as well, although with different viscous characteristics than the asphalt matrix itself. Figure 1a shows a photograph of the AC surface clearly illustrating the asphalt matrix (black regions) and aggregate (white/gray particles).

For this effort several AC mixes were prepared at the Advanced Transportation Research and Engineering Laboratory (ATREL) of the University of Illinois at Urbana-Champaign. Two types of materials were used in the study. The first type is AC mixes produced in a real production plant and sampled after production but before they were laid down in a pavement application. These mixes were brought to the lab and specimens were fabricated from them at ATREL. They are referred to as "Plant Mixes" hereafter. The second type is AC mixes prepared entirely in a laboratory environment by mixing aggregates and binder at conditions simulating plant production. These mixes are referred to as "Lab Mixes" hereafter. Standard procedures were followed for preparation of mixture sampling for plant and lab mixes (AASHTO 2013, 2012, 2014, 2015). Having mixes made in the laboratory specifically for this project enabled control of the composition (binder, aggregates and recycled content). Table 1 presents a summary of the AC mixes considered in this study. It presents the identification of the mixes and their major composition characteristics: binder performance grade (PG), RAS, recycled content (ABR) and AC.

Test specimen preparation was done by compacting both lab and plant AC mixtures at high temperature [approximately 140 °C (Ozer et al. 2012)] with a superpave gyratory compactor, which produced cylindrical samples of 150 mm diameter and 180 mm height according to the standard protocols (AASHTO 2015). Recently developed testing protocols were also fol-

Table 1 Summary of the asphalt mixes investigated

	LAB ID	Mix	PG	Slag (%)	RAP (%)	RAS (%)	ABR* (%)	AC (%)
Plant	P1	N50 SC	52-28	15	50	3.5	60	6.7
	P2	N50 SC	58-28	48	27	–	29	5.8
	P3	N70 BC	58-28	–	26	–	29	4.8
	P4	N30 BC	58-28	–	46.5	–	37	4.8
	P5	N70 SC	64-22	–	10	–	6	6.1
	P6	N90 SC	76-22	–	10	–	6	5.6
	P7	N50 SC	64-22	–	0	–	0	5.9
	P8	N50-50	58-28	–	42	4	49	5.5
LAB	L1	N90 CM 1 FG	70-22	–	–	–	–	6
	L2	N90 CM 2 FG	58-22	–	–	–	–	6
	L4	N90 CM 4 CG	64-22	–	–	–	–	6
	L6	N90 30 CG	58-28	–	–	7	29.8	6
	L7	N90 20 CG	58-28	–	–	5	21.2	6
	L8	N90 10 CG	64-22	–	–	2.5	10.5	6
	L9	N90-30-2 CG	64-22	–	–	7	29.8	6

* ABR $= \frac{Recycled\ asphalt\ binder\ (RAS\ or\ RAP)}{Total\ asphalt\ binder\ content} \times 100$ (Ozer et al. 2012)

lowed in preparation of bend fracture test specimens (AASHTO Provisional 2016). Specifically, these cylinders were cut in half perpendicular to the length and two slices were obtained after removing the top and bottom parts which were discarded as they are known to exhibit different mix distributions. Finally, each of these two middle slices was cut perpendicular to the thickness into two identical semicircular halves and an edge notch was made with a saw in the middle of the semi-circle base. The final specimen geometry tested was a semi-circular bend (SCB) specimen, shown schematically in Fig. 1b, with a diameter of 150 mm, thickness of 50 mm, notch length of 15 mm and notch width about 2 mm (the width of the saw).

2.2 Experimental set up

Experiments on AC SCB specimens were conducted at ATREL using an ITS Interlaken load frame, equipped with an environmental chamber to perform experiments at either −12 °C or 25 °C. All fracture experiments were displacement controlled with a constant displacement rate for loading from 0.1 to 50 mm/min depending on testing temperature. Load-line displacement (LLD) was the control variable for room temperature tests, while the crack mouth opening displacement (CMOD) was used at low temperature because it offers better stability for the growing crack: crack opening is at a constant rate which reduces the risk of having a crack propagating unstably through the specimen. For all experiments, the spacing between the two supports was 120 mm, as shown in Fig. 1b. Load and displacement data were acquired using the software UniTest (from Interlaken Technology Corporation), while pictures were recorded using the software VicSnap (from Correlated Solutions Inc.). The data analysis was done using the DIC software Vic2D (from Correlated Solutions Inc.), described in more detail below.

Digital images of the specimen surface were taken during every test using a charge couple device (CCD) camera (a Point Grey Gazelle 4.1 MP Mono, 2048 × 2048 pixels, 150 frames/s). These pictures were taken during the test so that the deformation of the specimen could be subsequently analyzed using the optical technique of digital image correlation (see Sect. 2.3 for more details). The experiments were conducted at several temperatures and loading rates to explore different aspects of the AC viscoelastic effect. Table 2 details the experiments conducted and test conditions used for each AC mix: temperature, rate, and the number of replicates tested. As can be seen this is a significant testing program over a wide range of material and conditions, and only a representative set of results will

Table 2 Summary of the SCB fracture experiments conducted

	LAB ID	Temperature (°C)	Rate (mm/min)	Replicates
Plant	P1	25	(6.25; 25; 50)	(3; 3; 3)
	P2	25	(6.25; 25; 50)	(3; 3; 3)
	P3	25	(6.25; 25; 50)	(3; 3; 3)
	P4	25	(6.25; 25; 50)	(3; 3; 3)
	P5	25	(6.25; 25; 50)	(3; 3; 3)
	P6	25	(6.25; 25; 50)	(3; 3; 3)
	P7	25	(6.25; 25; 50)	(3; 3; 3)
	P8	25	(6.25; 50)	(2; 2)
		−12	0.7	2
LAB	L1	25	(6.25; 25; 50)	(3; 3; 3)
	L2	25	(6.25; 25; 50)	(2; 2; 2)
	L4	25	6.25	3
			50	3
		−12	(0.1; 0.7)	(1; 2)
	L6	25	6.25	3
			50	3
		−12	(0.1; 0.7)	(1; 2)
	L7	25	(6.25; 50)	(3; 3)
	L8	25	6.25	3
			50	3
		−12	(0.1; 0.7)	(1; 2)
	L9	25	6.25	2
			50	2
		−12	0.7	2

be reported here in the interest of brevity. The reader is referred to Doll (2015) for more details on the experimental process and for a complete set of results.

As shown in Table 2, some experiments were done at (nominally) −12 °C. When experiments at this low temperature were conducted, the specimen had to be conditioned for several hours (usually overnight before the day of the experiment) to reach the desired temperature. Unfortunately, the door of the chamber was not transparent, so it was impossible to take pictures of the specimen with the environmental chamber active. Thus the chamber door had to be open while loading and consequently the chamber temperature was decreasing throughout the experiment which lasted approximately several minutes. To evaluate the temperature evolution of a specimen during the test, a dummy specimen which had a thermocouple embedded in it was used. The initial temperature when loading started was not −12 °C because of the time necessary to adjust the position and settings of the camera (the camera set-up could not be kept at the same place between two tests because it was obstructing the chamber door). The temperature increased monotonically during the test, reaching around 0 °C in about 17 min. However, most of our studies focus on the times before and immediately after peak load, which means that testing takes less than about *10 s* for the low temperature case. Thus the temperature can be considered effectively constant in this time duration, however not at a value of −12 °C. Although absolute consistency between experiments might not be assured, each specimen was effectively tested at isothermal conditions in the range between −10 and −7 °C depending on the time necessary to adjust the camera in each case. However, since we only compared low and elevated temperature experiments, i.e., −12 (nominally) and 25 °C, rather than compare between experiments at lower temperature, the precise value of the lower temperature in the range −10 to −7 °C does not affect the comparison. While keeping all this in mind, in the subsequent all the results from these experiments will be referred to as nominally at −12 °C.

2.3 Digital image correlation for use on asphalt material

DIC is an imaging technique that enables measurement of displacements and strains, and determination of stresses (the latter through appropriate constitutive equations) on the entire surface of a specimen, for the time instant corresponding to each picture taken (Sutton et al. 2009). DIC presents the advantage of being a non-contact full-field measurement technique and has been used for fracture or material characterization in many situations. For example, DIC has been used to study the mechanical and fracture properties of composites (Leclerc et al. 2009), metals (Carroll et al. 2013), functionally graded materials (Abanto-Bueno and Lambros 2002), concrete (Wu et al. 2011; Skarżyński et al. 2013) and asphalt (Seo et al. 2002; Buttlar et al. 2014).

To obtain the displacement field on the surface of a specimen, a reference picture is taken (usually at the unloaded state) of a random speckle pattern on the surface, and the pixels in a zone of interest are selected (Sutton et al. 2009). Then, subsets of pixels are com-

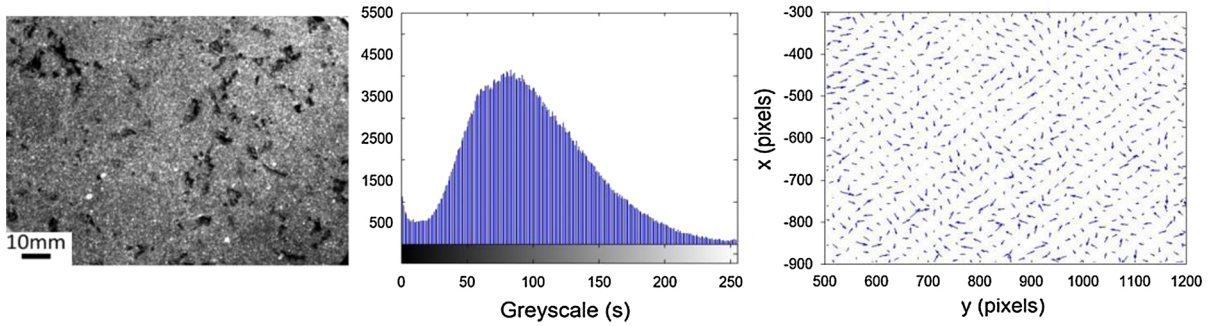

Fig. 2 Speckle pattern (*left*), grayscale intensity histogram (*middle*) and arrow plots denoting noise form correlation of two images without deformation (*right*) for the pattern used here

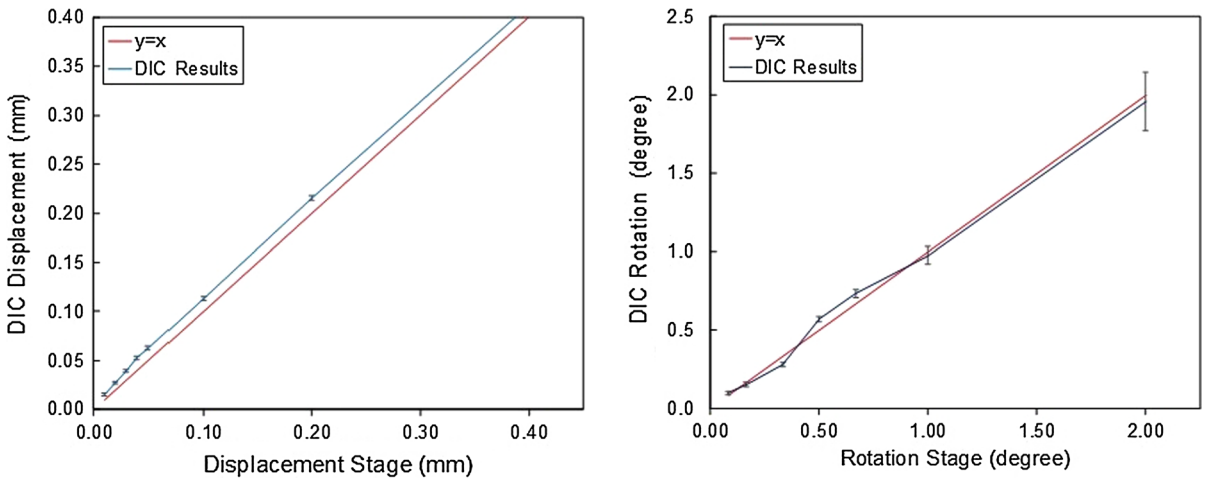

Fig. 3 DIC displacement versus imposed displacement horizontal translation (mm) on the *left*, rigid rotation (degrees) on the *right*

pared to a deformed picture (taken at a loaded state) to find a best match and thus compute the deformation of the subset, i.e., the displacement and the displacement gradients corresponding to the center of the subset. The main assumptions of DIC are the following: the deformation of each subset is assumed to be a homogeneous in-plane deformation and the specimen surface speckle pattern light intensity remains the same throughout deformation, which implies both light uniformity and no speckle deterioration.

For our study a suitable surface pattern was obtained by first applying a black layer of paint and then creating the speckle pattern by spraying white paint on top of it [i.e., in essence reversing the colors in the procedure of (Seo et al. 2002)]. Figure 2 shows a photo of a sample pattern using this method along with the intensity histogram, showing a unimodal intensity spectrum appropriate for DIC (Sutton et al. 2009). The noise level for the pattern obtained by correlating successive images of the same undeformed surface was: displacements measured around ± 0.01 mm and standard deviation around 0.006 mm, and appears random as seen in the arrow plot also shown in Fig. 2. The accuracy of resolving rigid body motion measurements was also investigated for the pattern before fracture experimentation. The results of known translation and rotation measurements are shown in Fig. 3 as DIC measurements (translation and rotation) versus imposed motion plots.

Another means to investigate the accuracy of DIC on AC when used in the Interlaken loading frame (which creates significant vibrations) was to compare the LLD measurements from the loading machine with the DIC measurements in the vicinity of load application. To measure as closely as possible the LLD with DIC, a "numerical gauge" was defined on the specimen, imme-

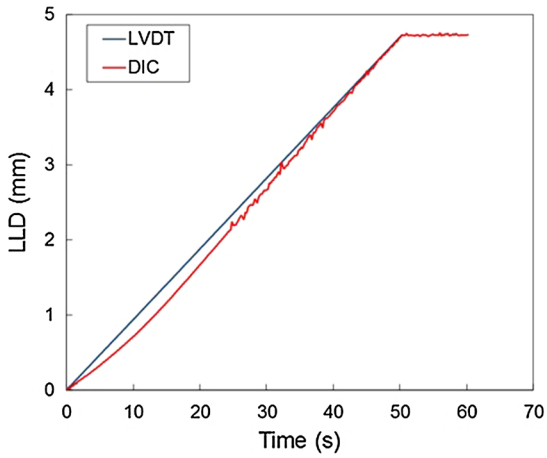

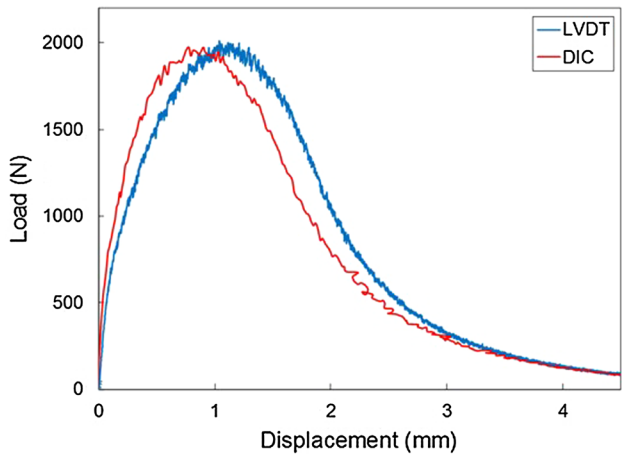

Fig. 4 LLD versus time (*left*) and load versus displacement (*right*) for the mix P7 at 6.25 mm/min. *Blue* displacements recorded with the load frame, *red* displacements measured with DIC at the subset location denoted by the *green box* in Fig. 1b. The small difference is due to the compliance of the loading fixtures

diately under the loading head (green box in Fig. 1b) and the evolution of its displacement was recorded. Figure 4 shows the comparison of the displacement versus time and the load versus displacement between the machine LLD measurement from the Interlaken LVDT and the corresponding "DIC computed LLD" for a typical AC mix at 6.25 mm/min. A good match between the two measurements is seen, which gives confidence in the use of DIC for fracture experiments with these testing conditions. Figures 5 and 6 show typical SCB fracture test results at different temperatures (25 and −12 °C) and rates (50 and 0.7 mm/min) respectively.

3 SCB deformation analysis

When measuring fracture energy from far-field load–displacement data fracture energy results are increasingly inaccurate if additional energy is dissipated in the specimen in regions far from the crack tip. The goal of the SCB is to localize most of the damage at the notch region and minimize other mechanisms of energy dissipation, such as crushing of the material near the loading region, or viscous/plastic bulk material dissipation. To investigate possible additional sources of energy dissipation, two areas of the SCB specimen geometry were studied more closely with DIC: the region near the load application point and the region surrounding the notch tip.

3.1 Investigation of possible load point damage

This part of the investigation was done on the seven plant AC mixes loaded at 6.25 and 50 mm/min. The progressive evolution of the horizontal strain, ε_{yy}, measured in the zone directly under the loading head is shown in Fig. 7. The load–displacement curve for the experiment is also shown, with the load level corresponding to the five strain plots indicated as a red dot on the load–displacement curve. To illustrate possible crushing under the loading head, the strain contours plotted are the negative ones (i.e., compressive) and all the positive strains are plotted in the same dark red color. The results did not show a strain field that could be interpreted as a crushing of the material. The area of the compressive zone was seen to develop as the load increased, reach a maximum after peak load and shrink, though still remaining larger than at peak load, as the crack propagated. (The crack location as a function of time in each image is shown by the blue dots in Fig. 7.) However, the magnitude of the strains kept increasing (in absolute value) all along the experiment. Our study did not observe any noticeable impact of the mixture or the loading rate (6.25 vs. 50 mm/min) on this effect. Primarily the development of the compressive region at the load point appears to be a specimen geometry effect: as the specimen bends, the lower part experienced tension while the top was compressed. When the crack propagated, the neutral axis for the bending strains moved further toward the top of the specimen and the compres-

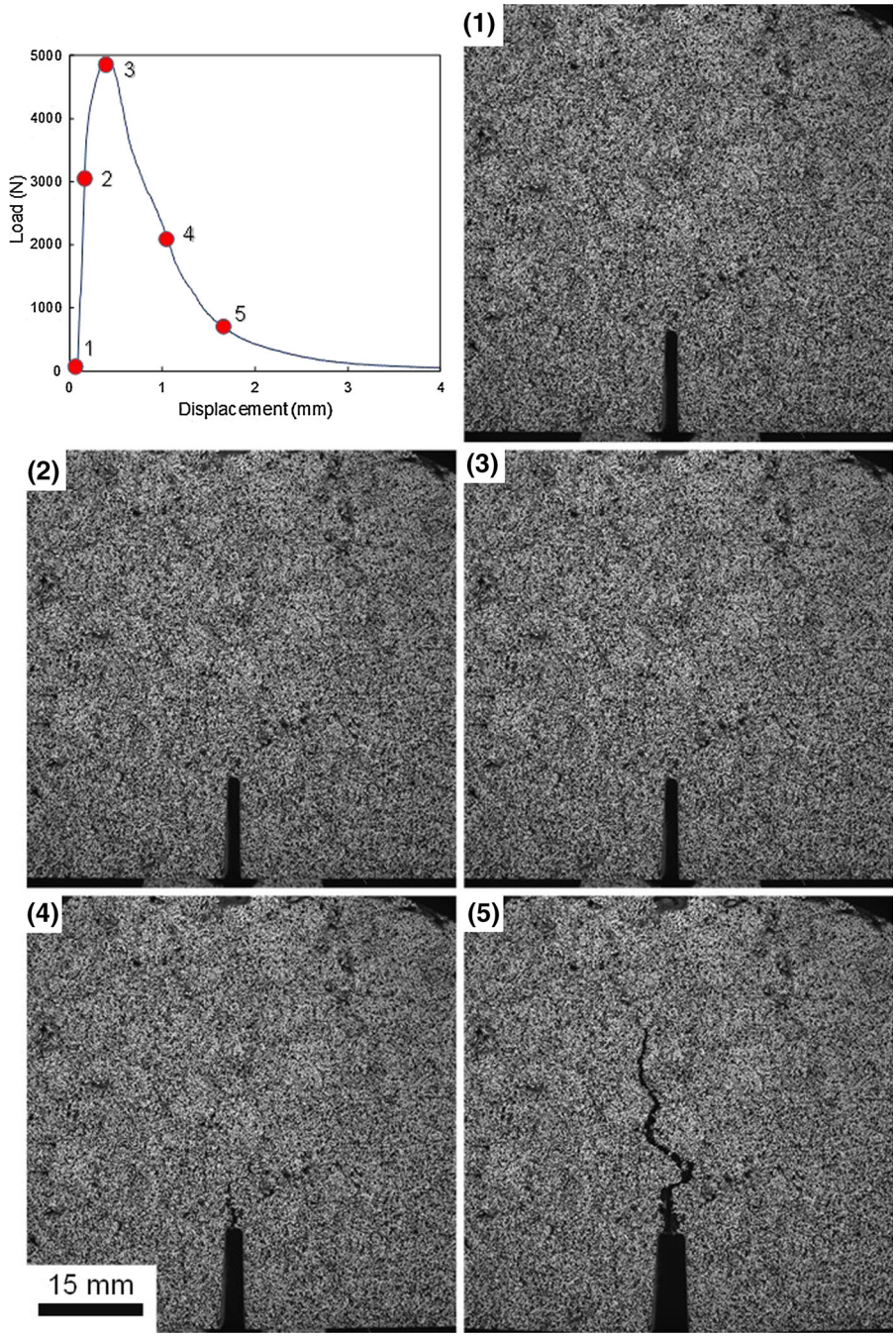

Fig. 5 Typical SCB fracture test images with corresponding load–displacement curve (mix L6 50 mm/min and 25 °C)

sive zone became smaller in extent although it increased in magnitude. Although no crushing was seen and the maximum strains recorded were less than the material failure strain, a large strain region could produce energy dissipation. However, the physical area over which the strains are large is confined to very near the loading pin, making the contribution to the global energy expended during the experiment a second order effect compared to fracture and bulk dissipation, discussed in the next section.

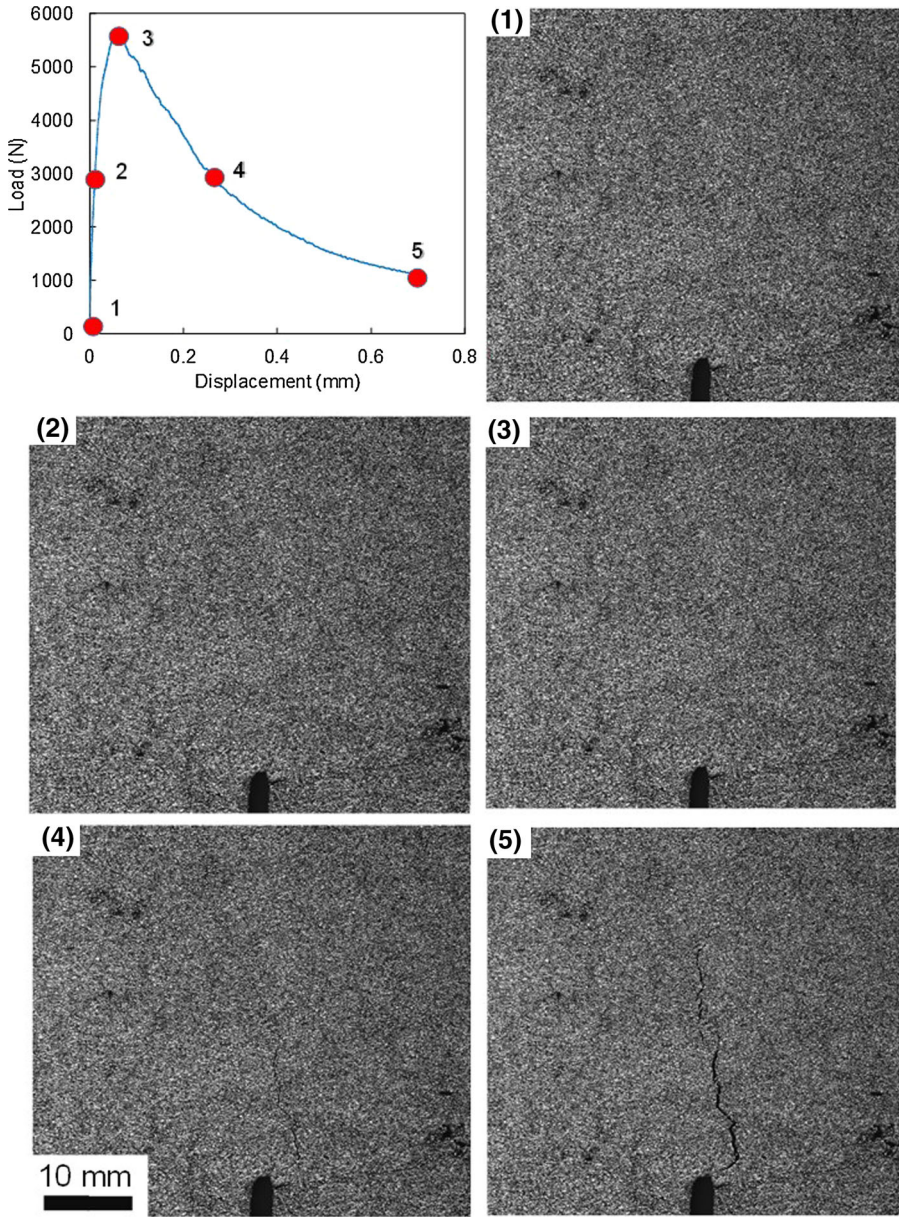

Fig. 6 Typical SCB fracture test images with corresponding load–displacement curve (N90-0 mix at 0.7 mm/min and −12 °C)

3.2 Bulk viscous dissipation

Asphalt concrete is a viscoelastic material, meaning that it exhibits some elastic characteristics, such as an instantaneous deformation behavior, and some viscous characteristics, such as a flow or time dependent behavior. This implies that there could be some bulk energy dissipation in the material when it is loaded which must be distinguished from the energy dissipated by fracture itself (i.e., the material inherent toughness). In addition, the material modulus cannot be considered a constant, which complicates the computation of a stress field from the DIC-measured strain field. As has been well developed in viscoelasticity theory, an integral representation for the constitutive response of viscoelastic media can be made using the following convolution equation (summation implied when indices are repeated):

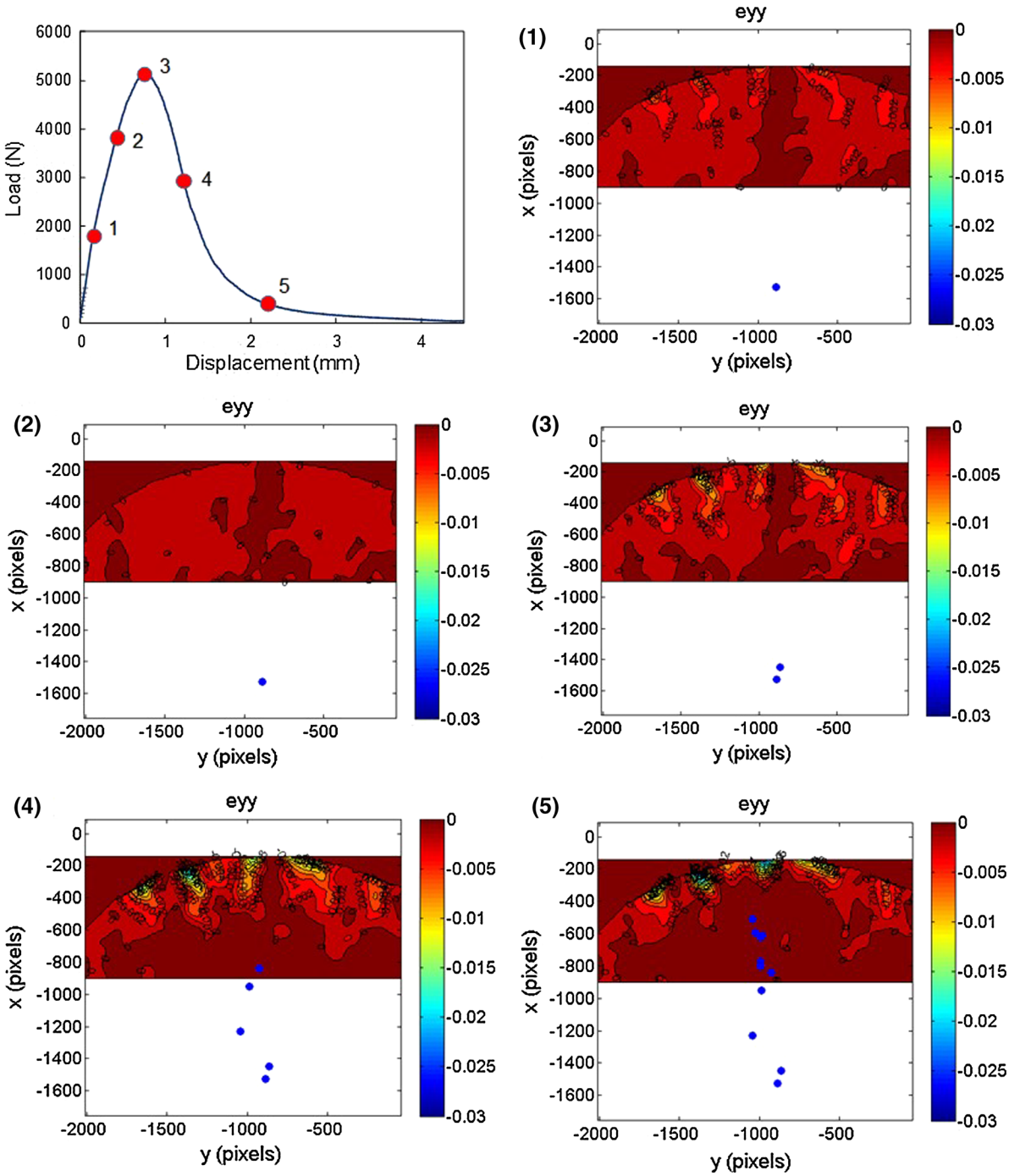

Fig. 7 Mix P6, 25 °C, 50 mm/min—evolution of compressive zone during a test. The scale shows only the compressive *horizontal* strains (tensile strains are in *dark red*). *Blue dots* successive locations of the notch or crack tip

$$\sigma_{ij}(\xi) = \int_0^{\xi} E_{ijkl}(\xi - \xi') \frac{\partial \varepsilon_{kl}(\xi')}{\partial \xi'} d\xi', \qquad (1)$$

where σ_{ij} and ε_{ij} are the stress and strain tensor components, E_{ijkl} are the time and temperature dependent stiffness modulus components, and ξ is a reduced

time defined for thermo-rheologically simple materials Christensen and Bonaquist (2012) as $\xi = \frac{t}{a_T}$, where a_T is a shift factor as defined by the Williams–Landel–Ferry (WLF) equation (Williams et al. 1955).

In our experiments where strain was measured as a function of load directly through DIC, stress history was calculated by computing the convolution integral in Eq. (1) at each load increment. In order to use Eq. (1), it is still necessary to explicitly know the temperature and time dependent modulus E, often represented in terms of a Prony series fit to experimental data as:

$$E(t) = E_e + \sum_{n=1}^{N} E_n e^{-t/\rho_n}, \tag{2}$$

where E_e is the equilibrium modulus, the E_n are the Prony coefficients and the ρ_n are the relaxation times. In our work we compute the Prony series from separate relaxation experiments performed for each mix. With these equations, it is then possible to compute stresses in the asphalt mix from measured strains.

In a fracture test, as the crack is propagating, the material is unloading behind it and strains decrease in the far-field (defined as the region outside any process zone). For an elastic material, the strains should return to their original unloaded state, except if some permanent deformation occurred such as in the process zone or a zone of (small scale) yielding. In viscoelastic materials, the far-field strains should recover also, but a complete recovery does not always happen, or may take a significant amount of time rather than happening instantaneously. This may provide another source of energy dissipation in the viscoelastic material that is not related to the fracture process itself.

To determine whether the contribution of such far-field bulk energy dissipation is significant in the AC case studies here we estimate local dissipation at specific locations in the bulk (i.e., away from the fracture process zone) we compute the area inside the stress–strain path experienced in a given region throughout the entire experiment, i.e., starting from the loading path as the crack approached the regions of interest and ending with the unloading and subsequent long term relaxation. As we neither have DIC strain measurements over the entire sample, which in any case would only provide in-plane not three dimensional strain information, nor do we know the precise extent of the fracture process zone near the tip, we cannot compute the actual total energy dissipated everywhere in the bulk. However calculating the area inside the stress–strain path at certain locations can provide an estimate of whether bulk dissipation need separately be considered or whether the "fracture" energy computed from far-field load–displacement calculations can reasonably be considered as entirely dissipated in the fracture process zone (as would be the case for a nominally brittle viscoelastic polymer for example). For an elastic response in the far-field, the area contained in the stress–strain hysteresis loop would be zero. The larger the area contained in a far-field stress–strain hysteresis loop, the more significant bulk dissipation. Since we cannot compute a total energy dissipated in each case, the results are subsequently used for a comparison between different mixes and/or loading conditions, rather than an absolute measure of bulk energy dissipated.

The local regions selected to illustrate such far-field dissipation calculations are shown in Fig. 8a as squares. This choice was made so that they represent areas larger than the aggregate size (to avoid local effects), but are sufficiently far away from the crack to be (mostly) outside the fracture process zone. As the DIC technique only provides measurement of in-plane displacement and strain components on the surface we assumed plane stress conditions on the surface in order to complete the three-dimensional picture of surface strain. Stresses were then computed from the DIC measurements using the viscoelastic constitutive Eq. (1). Note that this computation has to be done with the appropriate material Prony series properties, Eq. (2), *for each specific mix*. Therefore extensive constitutive testing had to be done to obtain relaxation moduli for each mix for which this viscoelastic computation is to be employed and the appropriate properties have to be used on a case by case basis (Al-Qadi et al. 2015). Typical local stress–strain paths obtained in this way for one mix, averaged over both regions of interest in Fig. 8a, from the three in-plane components (*xx*, *yy* and *xy*) are shown in Fig. 8b. The figure shows that the area enclosed in the opening component (*yy*) is the dominant one, so this component is the one used for the remaining results shown in this section. Far-field regions experience loading while the crack approaches them and unloading as the crack propagates beyond. During the loading and unloading cycle, some of the energy may be dissipated depending on the material properties. Although the curves shown in Fig. 8b are over the entire experiments, i.e., from ini-

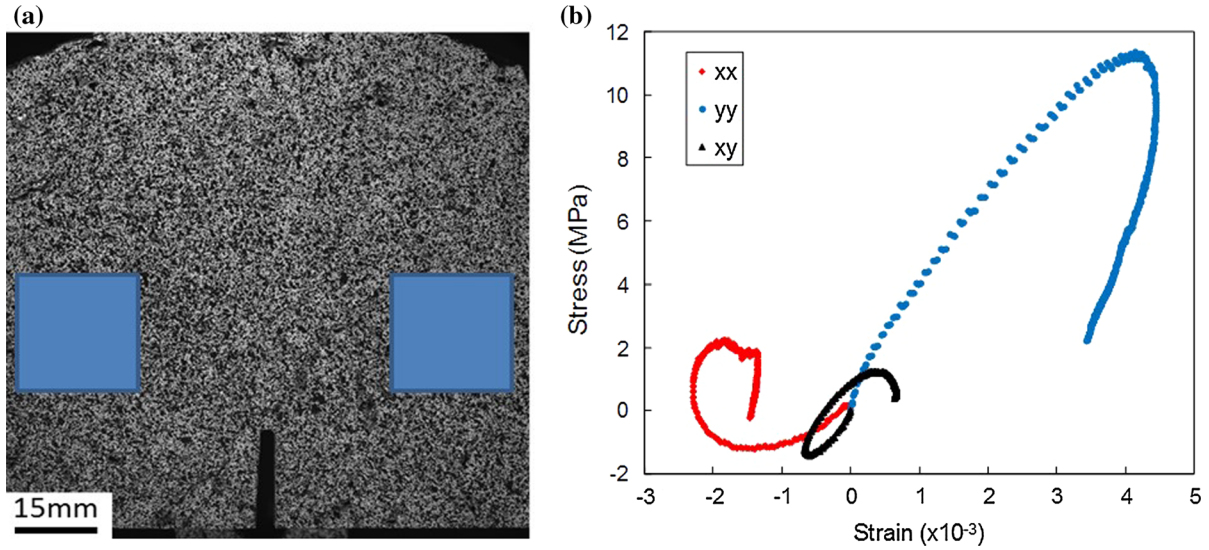

Fig. 8 **a** Areas over which far-field viscoelastic energy dissipation was computed. **b** Stress–strain path experienced in the areas shown in (**a**) shown individually for each in-plane component as labeled. Note that the total energy dissipated would be the summed area within each loop with the *xy* area multiplied by 2. Loading begins at the point (0, 0)

tial loading to complete sample failure, we have seen similar response in a series of experiments of partial unloading before crack initiation occurs, thus confirming bulk dissipation without the presence of fracture energy dissipation.

Several experiments were conducted at different rates with varying material viscoelastic characteristics. The average opening stresses–strain paths in these regions were computed for the mixes L4 (0% RAS), L7 (5% RAS) and L6 (7% RAS) (L7 and L6 have the same binder). For reference with the subsequent results, Fig. 9 shows the applied force–displacement results for each experiment at 6.25 and 50 mm/min at room temperature, illustrating good repeatability and good separation between cases. Figure 10a shows the effect of loading rate by comparing of the "loops" generated in the same mix (LAB mix L4) at 25 °C for 6.25 and 50 mm/min. The rate dependency is clearly highlighted here: at a higher rate, the strains decrease but the stresses increase.

To have a better understanding of the energy dissipated in the bulk of the material, the strain energy density W was computed as:

$$W = \int_0^{\varepsilon} \sigma_{ij} d\varepsilon_{ij}. \tag{3}$$

This energy is computed from all three strain components measured on the specimen surface, assuming a plane stress assumption on the surface, and the corresponding stresses competed form Eqs. (1–2), and the results are shown in Table 3 for the three mixes. The comparison of the average values for different loadingrates shows that there is a small increase of the energy dissipated as the loading rate increases, which is not obvious in Fig. 10a. This shows that the increase of the stresses with loading rate was more significant that the change in strains and was the reason for equivalent or more energy dissipation with increasing loading rate.

The same methodology was also used to compare the bulk energy dissipation with increasing RAS content. Figure 10b shows the stress–strain paths for the three mixes, two replicates each, at 6.25 mm/min. The curves corresponding to the same mix have a similar behavior, however the comparison between mixes shows a decrease of the area under the curve for increasing RAS content (see also same trend in dissipated energy in Table 3). This difference is particularly noticeable for mix L6 while the difference between mix L4 and L7 is smaller. This is due to the modification of the binder as a more compliant one was used for mixes L6 and L7 to compensate for the a priori expected embrittlement that would be introduced by RAS. It is still interesting to notice that the effects of increasing

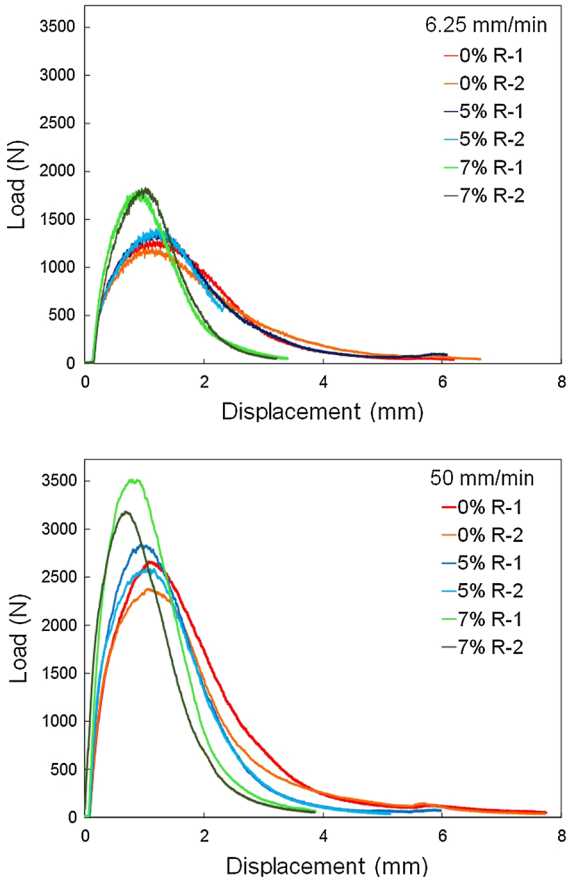

Fig. 9 Applied load–displacement plots for mixes L4 (0% RAS), L7 (5% RAS) and L6 (7% RAS) loaded at (*top*) 6.25 and (*bottom*) 50 mm/min. Two replicates of each shown

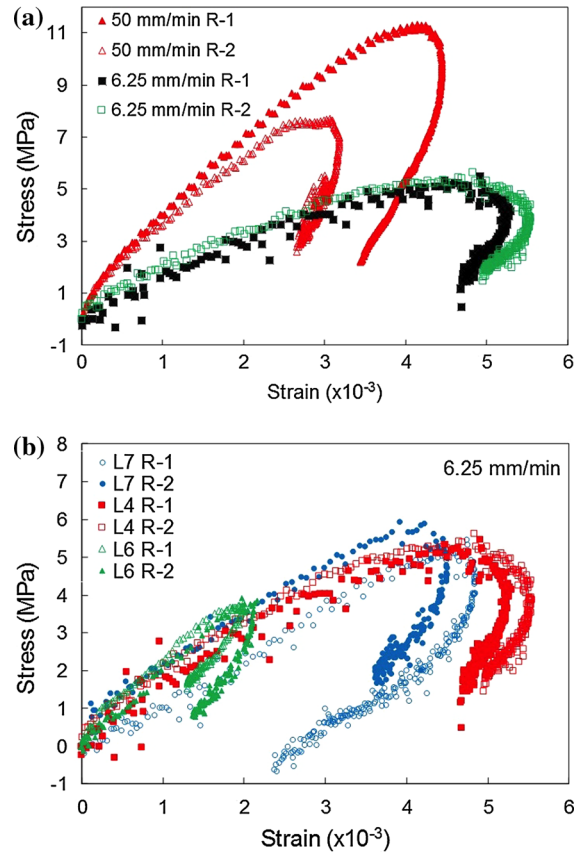

Fig. 10 **a** Stress versus strain for mix L4 at 25 °C and different rate comparison for two replicates at 50 and 6.25 mm/min. **b** Stress versus strain at 25 °C and 6.25 mm/min two replicates showing the effect of varying RAS content: L4 (0% RAS), L7 (5% RAS), L6 (7% RAS)

RAS content are counterbalanced by the composition of the binder when comparing mixes L4 and L7. However, the decrease of energy dissipation with increasing RAS still shows a loss of material viscosity. Figure 10b shows another interesting phenomenon: the difference between mixes is mostly due to differences in the strain levels.

4 Viscoelastic fracture analysis

Early works to describe fracture mechanisms for viscoelastic materials were primarily focused on the prediction of fracture toughness in polymers with varying crack speed and temperature. A comprehensive review of viscoelastic creep crack growth for poly-

Table 3 Strain energy density W for mixes L4, L7 and L6 at 6.25 and 50 mm/min (25 °C)

W (J/m^3)	6.25 mm/min			50 mm/min		
Replicate	1	2	Average	1	2	Average
L4 (0% RAS)	3.69E+04	3.42E+04	3.56E+04	2.80E+04	4.70E+04	3.75E+04
L7 (5% RAS)	2.04E+04	2.01E+04	2.03E+04	2.65E+04	2.24E+04	2.45E+04
L6 (7% RAS)	5.25E+03	5.9E+03	5.58E+03	9.33E+03	7.79E+03	8.56E+03

mers can be found in the work of Bradley et al. (1997) and in a recent review by Knauss (2015). A review of fracture theories and experiments was presented there to describe temperature and rate effects on the process zone. Initial attempts to understand experimental observations and formulate a valid theoretical framework centered around Griffith's surface energy concept. Knauss (1970) introduced the concept of delayed failure for linearly viscoelastic materials referring to the time effect on crack growth in polymeric materials. Knauss (1970, 1989) also showed that fracture and tensile failure behavior of some of the polymers obeys thermo-rheologically simple behavior, in which time and temperature effects can be superimposed with each other. Schapery in his early works also used a similar approach emanating from viscoelastic crack tip displacement fields and containment of failure to a very small crack tip region (Schapery 1975a, b, c). Singular crack tip equations were adopted for viscoelastic materials using convolution integrals and a compliance function. Christensen (1979) approached the viscoelastic crack growth problem using a different methodology: instead of imposing a particular crack tip failure criterion, this work attempted to generalize Griffith's energy balance method from global energy conservation laws and predicted motion of high and low speed velocity cracks in viscoelastic materials.

A common objective of the aforementioned works was to find a simple crack growth equation to describe rate and temperature dependent fracture for polymeric materials. However, these formulae containing the prediction of crack propagation speed were difficult to integrate into a numerical framework such as the finite element method. When compatibility of numerical and theoretical methodology was considered together, Schapery's generalized J-integral approach and pseudo variable concept for linear and nonlinear viscoelastic materials has been used extensively due to its practicality and similarity to Rice's J-integral approach (Schapery 1984, 1990; Rice 1968). Among the available models in the literature, Schapery's viscoelastic fracture model along with the elastic–viscoelastic correspondence principle provides an efficient platform to implement a viscoelastic fracture model that can be inserted into a finite element algorithm or post-process the displacement field obtained at a grid obtained from the DIC experiment. Schapery's model benefits from the framework of the classical J-integral and arrives at a work of fracture parameter to compute total work input to the crack tip considering viscoelastic effects. This approach was adopted in many applications to describe viscoelastic mechanisms for asphalt materials (Kim and Little 1990; Chehab et al. 2003, 2007; Underwood et al. 2012). Therefore, the approach outlined by Schapery and co-workers for viscoelastic fracture was also chosen in this paper.

Elastic–viscoelastic correspondence principles have been used to transform crack front parameters calculated in the corresponding elastic state to the viscoelastic domain (Ozer et al. 2011; Garzon 2013). The correspondence principle for viscoelastic materials states that viscoelastic problems can be decomposed into a reference linear elastic solution and a viscous solution, assuming that the elastic and viscoelastic bodies are geometrically identical (Schapery 1984) and assuming that they undergo the same stress,

$$\sigma_{ij}^R = \sigma_{ij}^V = \sigma_{ij}, \tag{4}$$

where the superscript "R" denotes the reference elastic solution, the superscript "V" denotes the viscous solution, and no superscript is the total state. The reference (elastic) variables, sometimes called *pseudo-variables*, are denoted as $\sigma_{ij}^R, \varepsilon_{ij}^R$ and u_i^R. The pseudo elastic state satisfies the usual equations of elasticity. The total and pseudo strains and displacements are related by (Schapery 1989):

$$\varepsilon_{ij} = E^R \int_0^t D\left(t - t'\right) \frac{\partial \varepsilon_{ij}^R}{\partial t'} dt', \tag{5}$$

$$\varepsilon_{ij}^R = \frac{1}{E^R} \int_0^t E\left(t - t'\right) \frac{\partial \varepsilon_{ij}}{\partial t'} dt', \tag{6}$$

$$u_i = E^R \int_0^t D\left(t - t'\right) \frac{\partial u_i^R}{\partial t'} dt', \tag{7}$$

$$u_i^R = \frac{1}{E^R} \int_0^t E\left(t - t'\right) \frac{\partial u_i}{\partial t'} dt', \tag{8}$$

The viscous part of the problem is then found easily assuming an additive decomposition of total strains and displacements:

$$\varepsilon_{ij} = \varepsilon_{ij}^R + \varepsilon_{ij}^V, \tag{9}$$

$$u_i = u_i^R + u_i^V. \tag{10}$$

E^R in Eqs. (5)–(10), the reference modulus, is an arbitrary value often chosen as the instantaneous modulus

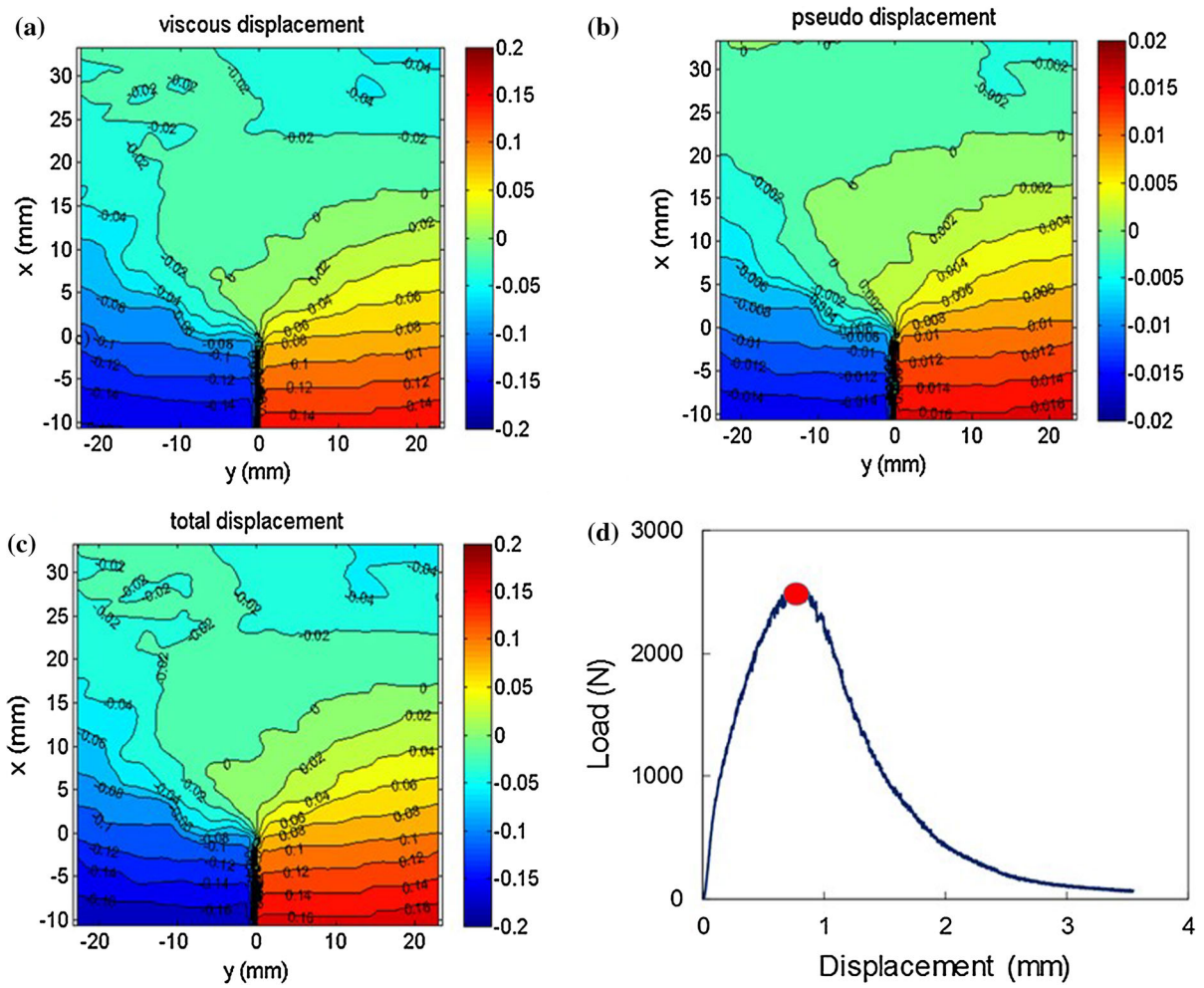

Fig. 11 Mix P1 at 25°C, 6.25 mm/min, horizontal displacement decomposition. **a** Viscous, **b** pseudo, **c** total, **d** load–displacement, the *red dot* indicates the load for this picture. Note the *contour scales in each plot*

$E_0 \left(= \sum_{n=1}^{N} E_n + E_e\right)$ (Ozer et al. 2011; Tabatabaee and Bahia 2014).

The correspondence principle enables decomposing displacements or strains into their viscous and elastic parts, making possible the comparison of the contribution of each component to the material behavior for different loading conditions. Using this approach, the pseudo and viscous displacement or strains were computed on the surface of the specimens based on the DIC measurements performed and the appropriate material properties for each mix. Figure 11 shows one example result at peak load for mix P1 loaded at 25 °C and at 6.25 mm/min. The horizontal displacements (viscous, pseudo and total) are plotted in the three contour plots shown in Fig. 11. It should be noted that the rigid body motions were not removed from the displacement field. However, those contour plots generally correspond to the expected opening field for mode I crack opening. The three contour plots present a similar distribution of the displacements; the major difference between them is in the displacement scale. The elastic part represents a small fraction of the total displacements: the contribution of the elastic components (strain and displacement) is between 20 and 10% of the total amount, decreasing along the duration of the experiment as the viscous effects develop in the material over time. This could perhaps be expected from the viscoelastic characteristic of AC material at intermediate temperatures for this

particular mix. According to the viscoelastic characterization of this particular mix and similar ones, the modulus of the mix [not shown here but available in Doll (2015)] decreases by a factor of ten in about one second indicating the relaxation potential of the material. It is worth pointing out that when the same decomposition is made for the low temperature experiments (at −12 °C) the opposite result is obtained (not shown): the elastic content dominates the displacement and strain and the viscous portion is less than 10% of the total. Thus we would expect more of an elastic behavior in the low temperature experiments, as is usually the case for viscoelastic materials.

This study ultimately focuses on the fracture properties of AC, using both virgin binder and binder with recycled content. The (mode I) stress intensity factor K_I has been introduced in linear elastic fracture mechanics (LEFM) to characterize the stress, strain and displacement fields surrounding an opening crack in a linearly elastic material. For mode I opening, the asymptotic (i.e., near the tip) elastic displacement field is described to first order by the following equations (Williams 1957)

$$\left\{\begin{matrix} u_x \\ u_y \end{matrix}\right\} = \frac{K_I}{2\mu}\sqrt{\frac{r}{2\pi}} \left\{\begin{matrix} \cos\left(\frac{\theta}{2}\right)\left[\kappa - 1 + 2\sin^2\left(\frac{\theta}{2}\right)\right] \\ \sin\left(\frac{\theta}{2}\right)\left[\kappa + 1 - 2\cos^2\left(\frac{\theta}{2}\right)\right] \end{matrix}\right\} + \left\{\begin{matrix} u_{x0} - \theta_0 y \\ u_{y0} + \theta_0 x \end{matrix}\right\}, \quad (11)$$

where $\kappa = 3-4\nu$ for plane strain or $\kappa = \frac{3-\nu}{1+\nu}$ for plane stress, ν is the Poisson ratio, μ the shear modulus, u_{x0} and u_{y0} correspond to the rigid translation and θ_0 is the rigid translation.

The DIC analysis extracts the displacement field from the pictures taken during the experiments and, for the elastic case, it is then possible to do a least squares regression of the DIC-measured displacements on Eq. (11) to compute K_I. In the viscoelastic case, the same method cannot be used directly on the DIC measurements but requires using the *pseudo displacements* in Eq. (11). Then, if required, viscoelastic crack front parameters can be found using Laplace transformations. It is important to note this transformation is essential as the stress intensity factor extraction methods are developed for linear elasticity and time independent materials and cannot be used directly for viscoelastic materials. Therefore, we will compute what is denoted as K_I^R, the "pseudo" stress intensity factor, which corresponds to the stress intensity factor for an equivalent elastic problem with a modulus E^R (Schapery 1989). In essence this approach extracts the elastic portion of the measured displacement field and uses that in the computation of the pseudo stress intensity factor. The procedure in this case, therefore, is to measure the DIC displacements from the pictures using the software Vic2D, then use these DIC displacements, the Prony series of the material, and the time step between each picture to compute the pseudo displacements from Eq. (8), and then do a least squares regression on the pseudo displacements using Eq. (11), which then produces K_I^R and the rigid body motion amount. This procedure is done for a number of different mixes tested at room temperature and low temperature, over various loading rates, and with varying amounts of recycled content.

Figure 12 shows the comparison between K_I^R, measured as discussed above, and the theoretical K_I, which is calculated for the SCB geometry as discussed in the work of Lim et al. (1993), for varying AC mixes with RAS contents at loading rates of 6.25 and 50 mm/min. Figure 12a shows the load–displacement curves of the SCB AC samples used in this part of the study—each case showing very good agreement between two replicates. Figure 12b, c shows the pseudo stress intensity factor comparison with the purely elastic predictions for a loading rate of 6.25 and 50 mm/min, respectively. The experimental results shown in Fig. 12a, b are only up to the time of crack initiation in each case, which is why the data points end at different load levels in each case. The first observation is that the pseudo stress intensity factor, K_I^R, diverges from the theoretical one as the loading increases for all materials. In both rate cases for AC with virgin binder (denoted 0% in the figure), the measured results do not agree well with the 2D elastic result even when the loads are small at the beginning of the experiment. However, agreement is improved as RAS content is added, which is a result of the embrittlement of the material, or reducing viscous components, with increasing RAS additions. (This embrittlement is also seen directly in the load–displacement curves of Fig. 12a which show an increased peak load but much less ductility as RAS content increases). For higher RAS content the stress intensity factor comparison is favorable until about 800 N in the 6.25 mm/min case and 1200 N in the 50 mm/min one. The results of comparing the measured pseudo stress intensity factor and the theoretical one indicate a combination of a strong influence of viscoelasticity at the intermediate temperatures and the potential for a distributed damage process at the crack front which

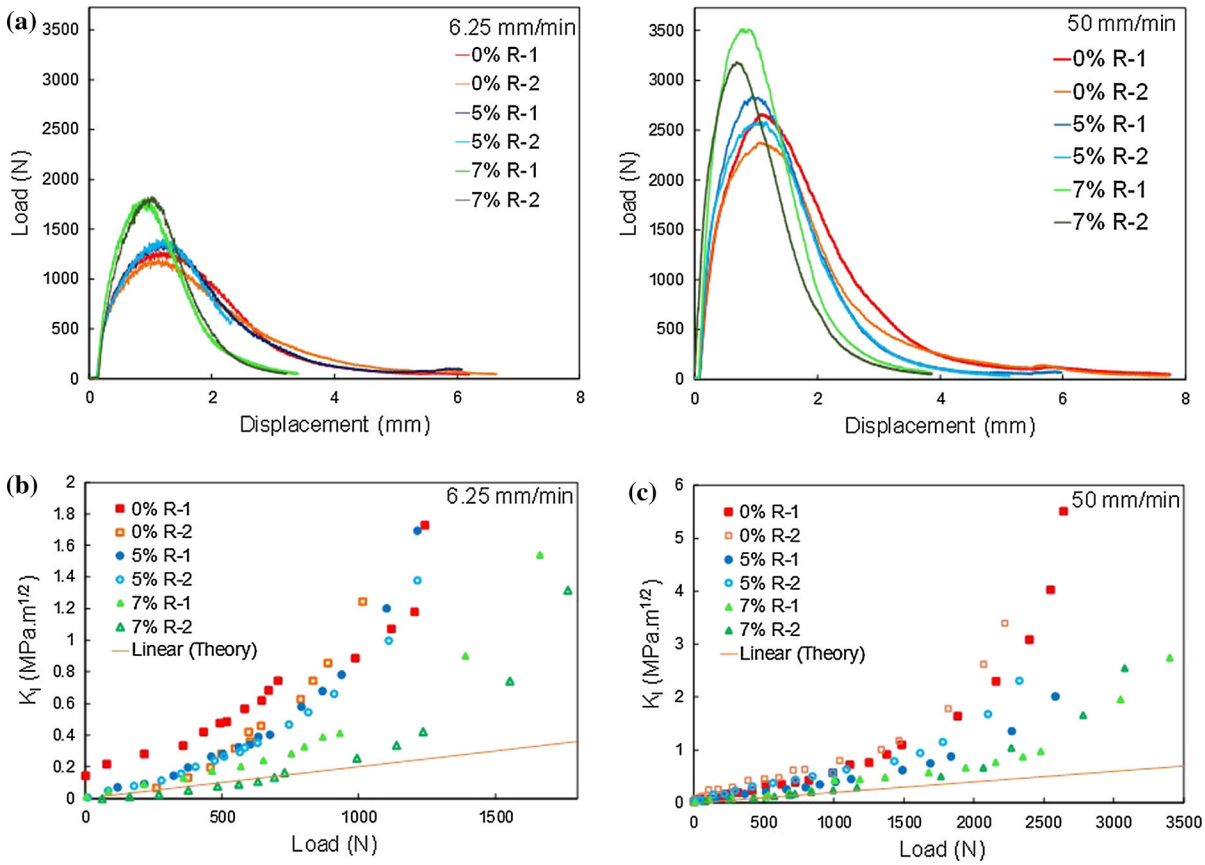

Fig. 12 **a** Typical load versus displacement curves for loading at 6.25 (*left*) and 50 mm/min (*right*) at room temperature, **b** extracted pseudo stress intensity factor versus load for different RAS content mixes at 6.25 mm/min and 25 °C and **c** extracted pseudo stress intensity factor versus load for different RAS content mixes at 50 mm/min and 25 °C

cannot be explained or accounted for by the LEFM stress intensity factor concept alone.

The values obtained are also consistent with values of room temperature fracture toughness measured previously for AC: around 0.5–1.5 MPa$\sqrt{m}$ (Kim and El Hussein 1997; Marasteanu et al. 2002). After these limits the results start diverging, denoting a nonlinear contribution to the pseudo-elastic part, and also a collapse of any region of K-dominance around the notch tip, both of which are expected to occur as load is increased and/or the crack grows. In fact the point at which the results diverge from the 2D theoretical result is in all cases when the crack has grown a substantial amount through the specimen and the remaining ligament is then fully damaged.

Figure 13 shows a similar set of results for a fixed specific mix (N90-0) but now varying with loading rate and temperature. Experimental results shown are again for loads prior to crack initiation. The embrittlement of the material with decreasing temperature is seen in both the load–displacement curve (Fig. 13a) and in the far better comparison of the pseudo stress intensity factor with the theoretical elastic solution (Fig. 13b). Recall also that in the low temperature case the pseudo displacements are about 90% of the total displacements (rather than the reverse ratio at the room temperature case) meaning that most of the displacement field has elastic character anyway. (In fact computing the stress intensity factor with the compete DIC-measured displacement field rather than the pseudo one for the −12 °C case produces about the same values as shown in Fig. 13b). Therefore, the temperature induced embrittlement is clear in Fig. 13b and can be compared to the rate induce embrittlement (shown in

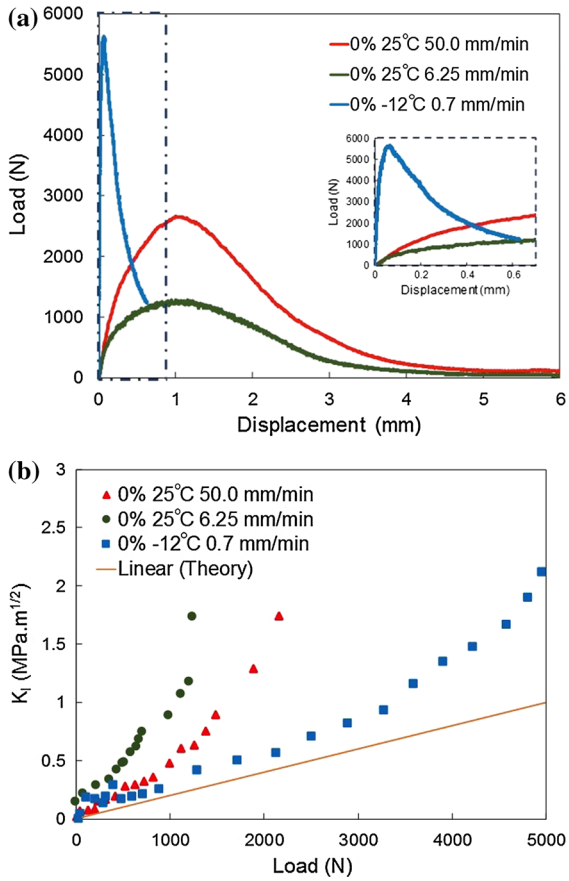

Fig. 13 **a** Typical load versus displacement curves and **b** extracted pseudo stress intensity factor versus load for N90-0 Mix at 50 mm/min (25 °C), 6.25 mm/min (25 °C) and 0.7 mm/min (−12 °C)

Fig. 12b) and the RAS induced embrittlement (shown in Fig. 12c).

5 Conclusions

The amount of recycled content (RAS and RAP) added in new asphalt concrete (AC) pavements is continually increasing as it represents both initial cost savings and conservation of natural resources. However, recycled content affects the resulting material properties as some virgin binder is replaced with aged binder whose characteristics are not well determined and/or known. There is, therefore, a need to understand the effects of recycled content added to the mixture and evaluate the performance of AC depending on level of recycled content.

The experiments conducted here allowed us to compute the viscoelastic counterpart (pseudo-elastic quantities) of the stress intensity factor, using the elastic–viscoelastic correspondence principle for fracture experiments on AC both at room temperature and at −12 °C. Regarding possible sources of energy dissipation away form the crack tip region, it was shown that:

- No obvious crushing of the material could be observed under the SCB loading head. However, a zone of compressive strains was developing, which is loading rate and mix independent but governed by bending of the specimen.
- Stress–strain response in the far-field regions was used to quantify local energy dissipation which may not be related to the fracture processes. It was shown that material type (represented by binder grade), recycled content, and rate of loading played a role in the energy dissipated in the far-field regions.
- The far-field loading and unloading of the mixes showed that an increasing RAS content induced a faster unloading rate and more strain recovery, which corresponds to a less viscous behavior, and is consistent with the findings from the viscous strains. Therefore, an increasing RAS content induces a decrease in the energy dissipated indicating less viscous characteristics of these mixes with increasing RAS. However, using a softer binder (more viscous) in the preparation of the mix can compensate for the effects of RAS concerning the energy dissipated in the far-field regions and the two binders blend.

In addition, regarding the fracture response it was shown that:

- The elastic–viscoelastic correspondence principle can be used to decompose elastic and viscous contributions to the crack front parameters for different asphalt mixes. The K_I^R (reference, or pseudo, elastic stress intensity factor computed from the viscoelastic response) and theoretical stress intensity factor were compared at different rates, for different mixes with varying degrees of viscoelasticity, and at different temperatures (−12 and 25 °C). In general, the K_I^R and theoretical stress intensity factor are in good agreement at the beginning of the test when the loads are small and for less viscoelastic

materials (such as the ones with increasing recycled content or at lower temperature).

- The effect of RAS was evident in the global load–displacement curves and the crack front parameters. Embrittlement and increasing stiffness of the mixes can be observed by the increase in the peak load, increase in the initial stiffness, and reduction in the displacement to reach peak load. With the decreasing viscous components and increasing stiffness, the mixes with increasing RAS content showed some correlation to the theoretical stress intensity factor when the loads are up to about 800 N. For such mixes, it can be hypothesized that fracture process zone may still be small and have smaller viscous component of deformations indicating increased brittleness, similar to low temperature response.

As a counterpart of this study, similar DIC experiments were conducted with higher resolution cameras (8 μm/pixel rather than the 40 μm/pixel used here) with an objective to evaluate the hypothesis explaining the discrepancy between theoretical and pseudo stress intensity factors. Material heterogeneity and damage processes at the crack front will be explored using the DIC technique utilizing high resolution cameras in a future contribution (Doll et al. 2016).

Acknowledgements Support for this study was provided by the Illinois Department of Transportation (IDOT) as part of the ongoing ICT R27-128 research project. The authors would like to acknowledge the members of IDOT Technical Review Panel (TRP) for their useful advice at different stages of this research. The contents of this paper reflect the views of the authors who are responsible for the facts and the accuracy of the data presented herein. This paper does not constitute a standard, specification, or regulation. We would also like to thank Ahmad El Khatib, Punit Singhvi, Tamim Khan for their help with preparing and characterizing asphalt concrete samples, and Erman Gungor for providing some Matlab codes. BD and JL would also like to thank the Institut Supérieur de l'Aéronautique et de l'Espace (ISAE – Supaero) in France which gave BD the opportunity to join the University of Illinois as part of a dual degree program.

References

AASHTO T 166 (2013) Standard method of test for bulk specific gravity (GMB) of compacted hot mix asphalt (HMA) using saturated surface-dry specimens. American Association of State and Highway Transportation Officials

AASHTO T 209 (2012) Standard method of test for theoretical maximum specific gravity (GMM) and density of hot mix asphalt (HMA). American Association of State and Highway Transportation Officials

AASHTO T 269 (2014) Standard test method for percent air voids in compacted dense and open asphalt mixtures. American Association of State and Highway Transportation Officials

AASHTO T 312 (2015) Standard method of test for preparing and determining the density of asphalt mixture specimens by means of the superpave gyratory compactor. American Association of State and Highway Transportation Officials

AASHTO Provisional (2016) Flexibility index for overall fracture resistance of asphalt mixtures using semicircular bend geometry (SCB). American Association of State and Highway Transportation Officials (in revision)

Abanto-Bueno J, Lambros J (2002) Investigation of crack growth in functionally graded materials using digital image correlation. Eng Fract Mech 69:14–16

Ahmedzade P, Sengoz B (2009) Evaluation of steel slag coarse aggregate in hot mix asphalt concrete. J Hazard Mater 165:300–305

Al-Qadi IL, Ozer H, Lambros J, EL-Khatib A, Singhvi P, Khan T, Rivera-Perez J, Doll B (2015) Testing protocols to ensure performance of high asphalt binder replacement mixes using RAP and RAS. Report no. FHWA-ICT-15-017, Illinois Center for Transportation, Rantoul, IL

Buttlar WG, Hill BC, Richard Kim Y, Kutay ME, Millien A, Montepara A, Paulino GH, Petit C, Pop IO, Romeo E, Roncella R, Safavizadeh SA, Tebaldi G, Wargo A (2014) Digital image correlation techniques to investigate strain fields and cracking phenomena in asphalt materials. Mater Struct 47(8):1373–1390

Bradley W, Cantwell WJ, Kausch HH (1997) Viscoelastic creep crack growth: a review of fracture mechanical analyses. Mech Time-Depend Mater 1(3):241–268

Carroll JD, Abuzaid W, Lambros J, Sehitoglu H (2013) High resolution digital image correlation measurements of strain accumulation in fatigue crack growth. Int J Fatigue 57:140–150

Chehab GR, Kim YR, Schapery RA, Witczak MW, Bonaquist R (2003) Characterization of asphalt concrete in uniaxial tension using a viscoelastoplastic continuum damage model. In: Association of asphalt paving technologists technical sessions, vol 72. Lexington, Kentucky, USA

Chehab GR, Seo Y, Kim YR (2007) Viscoelastoplastic damage characterization of asphalt-aggregate mixtures using digital image correlation. Int J Geomech 7(2):111–118

Christensen RM (1979) A rate-dependent criterion for crack growth. Int J Fract 15(1):3–21

Christensen DW, Bonaquist R (2012) Modeling of fatigue damage functions for hot mix asphalt and application to surface cracking. Road Mater Pavement Des 13:102–123

Doll B (2015) Evaluation of viscous effects in crack tip fields in recycled asphalt pavement materials using digital image correlation. MS thesis, University of Illinois

Doll B, El Khatib A, Ozer H, Al-Qadi IL, Lambros J (2016) Fracture process zone development in heterogeneous asphalt materials. Eng Fract Mech **(in preparation)**

Garzon TJ (2013) Three-dimensional numerical analysis of reflective cracks in airfield pavements. Doctoral dissertation, University of Illinois at Urbana-Champaign

Goh SW, You Z (2011) Evaluation of recycled asphalt shingles in hot mix asphalt. Transportation and Development Institute Congress

Gorkem C, Sengoz B (2009) Predicting stripping and moisture induced damage of asphalt concrete prepared with polymer modified bitumen and hydrated lime. Constr Build Mater 23:2227–2236

Johnson E, Johnson G, Dai S, Linell D, McGraw J, Watson M (2010) Incorporation of recycled asphalt shingles in hot mixed asphalt pavement mixtures. Minnesota Department of Transportation, Office of Policy Analysis, Research and Innovation, 2010 report

Kim YR, Little DN (1990) One-dimensional constitutive modeling of asphalt concrete. J Eng Mech 116(4):751–772

Kim KW, El Hussein M (1997) Variation of fracture toughness of asphalt concrete under low temperatures. Constr Build Mater 11:7–8

Knauss WG (1970) Delayed failure-griffith problem for linearly viscoelastic materials. Int J Fract 6(1):7–20

Knauss WG (1989) Time dependent fracture of polymers. Adv Fract Res 4:2683–2711

Knauss WG (2015) A review of fracture in viscoelastic materials. Int J Fract 196(1–2):99–146

Leclerc H, Perie JN, Roux S, Hild F (2009) Integrated digital image correlation for the identification of mechanical properties. Computer vision/computer graphics collaboration, techniques lecture notes in computer science, vol 5496

Lim IL, Johnston IW, Choi SK (1993) Stress intensity factors for semi-circular specimens under three-point bending. Eng Fract Mech 44(3):363–382

Marasteanu MO, Dai S, Labuz JF, Li X (2002) Determining the low-temperature fracture toughness of asphalt mixtures. Transp Res Rec 1789:191–199

Masad E, Somadevan N, Bahia HU, Kose S (2001) Modeling and experimental measurements of strain distribution in asphalt mixes. J Transp Eng 127(6):477–485

Newcomb D, Stroup-Gardiner M, Weikle B, Drescher A (1993) Influence of roofing shingles on asphalt concrete mixture properties. Report 93/09 Submitted to Minnesota Department of Transportation, Office of Research Administration

Osman MO (2014) Special provision for reclaimed asphalt pavement (RAP) and reclaimed asphalt shingles (RAS). Illinois Department of Transportation, Bureau of Materials and Physical Research, report 80306m

Ozer H, Al-Qadi IL, Duarte CA (2011) Effects of non uniform and three-dimensional contact stresses on near-surface cracking. Transportation Research Record: Journal of the Transportation Research Board, No. 2210

Ozer H, Al-Qadi IL, Kanaan A (2012) Laboratory evaluation of high asphalt binder replacement with recycled asphalt shingles (RAS) for a low N-design asphalt mixture. Illinois Center for Transportation, report ICT-R27-SP19

Petersen JC, Harnsberger PM (2007) Asphalt aging: dual oxidation mechanism and its interrelationships with asphalt composition and oxidative age hardening. Transportation Research Record: Journal of the Transportation Research Board, vol 1638

Rice JR (1968) A path independent integral and the approximate analysis of strain concentration by notches and cracks. J Appl Mech 35(2):379–386

Schapery RA (1975a) A theory of crack initiation and growth in viscoelastic media. Int J Fract 11(1):141–159

Schapery RA (1975b) A theory of crack initiation and growth in viscoelastic media II—approximate methods of analysis. Int J Fract 11(3):369–388

Schapery RA (1975c) A theory of crack initiation and growth in viscoelastic media III—analysis of continuous growth. Int J Fract 11:549–562

Schapery RA (1984) Correspondence principles and a generalized J integral for large deformation and fracture analysis of viscoelastic media. Int J Fract 25(3):195–223

Schapery RA (1989) On the mechanics of crack closing and bonding in linear viscoelastic media. Int J Fract 39(1):163–189

Schapery RA (1990) On some path independent integrals and their use in fracture of nonlinear viscoelastic media. Int J Fract 42(2):189–207

Seo Y, Kim Y, Witczak M, Bonaquist R (2002) Application of digital image correlation method to mechanical testing of asphalt–aggregate mixtures. Transportation Research Record: Journal of the Transportation Research Board, vol 1789

Skarżyński L, Kozicki J, Tejchman J (2013) Application of DIC technique to concrete–study on objectivity of measured surface displacements. Exp Mech 53(9):1545–1559

Sutton MA, Orteu JJ, Schreier H (2009) Image correlation for shape, motion and deformation measurements: basic concepts: theory and applications. Springer, New York

Tabatabaee HA, Bahia HU (2014) Establishing use of asphalt binder cracking tests for prevention of pavement cracking. Road Mater Pavement Des 15(1):279–299

Underwood B, Baek C, Kim Y (2012) Simplified viscoelastic continuum damage model as platform for asphalt concrete fatigue analysis. Transportation Research Record: Journal of the Transportation Research Board, vol 2296, pp 36–45

Williams ML, Landel R, Ferr J (1955) The temperature dependence of relaxation mechanisms in amorphous polymers and other glass-forming liquids. J Am Chem Soc 77(14):3701–3707

Williams ML (1957) On the stress distribution at the base of a stationary crack. J Appl Mech 24:109–114

Wu ZM, Rong H, Zheng JJ, Xu F, Dong W (2011) An experimental investigation on the FPZ properties in concrete using digital image correlation technique. Eng Fract Mech 78:2978–2990

Zhao S, Bowers B, Huang B, Shu X (2014) Characterizing rheological properties of binder and blending efficiency of asphalt paving mixtures containing RAS through GPC. J Mater Civ Eng 26(5):941–946